IEEE Access
Multidisciplinary | Rapid Review | Open Access Journal

Received April 4, 2022, accepted May 9, 2022, date of publication May 17, 2022, date of current version May 26, 2022.

Digital Object Identifier 10.1109/ACCESS.2022.3175840

Ultra-Wideband Coplanar Vivaldi Antenna Array With Dielectric Patch Antenna for Grating Lobes Suppression

FERAS ABUSHAKRA[1], NATHAN JEONG[1], (Senior Member, IEEE), ABHISHEK K. AWASTHI[1,2], (Member, IEEE), SHRINIWAS KOLPUKE[3], (Graduate Student Member, IEEE), CHRISTOPHER SIMPSON[3], OMID REYHANIGALANGASHI[1], (Graduate Student Member, IEEE), DEEPAK N. ELLURU[1], (Graduate Student Member, IEEE), AABHASH BHANDARI[3], DREW TAYLOR[1], (Member, IEEE), AND S. PRASAD GOGINENI[1,3], (Life Fellow, IEEE)

[1]Department of Electrical and Computer Engineering, The University of Alabama, Tuscaloosa, AL 35487, USA
[2]Department of Electrical and Electronics Engineering, School of Engineering, University of Petroleum and Energy Studies (UPES), Dehradun 248007, India
[3]Department of Aerospace Engineering and Mechanics, The University of Alabama, Tuscaloosa, AL 35487, USA

Corresponding author: Feras Abushakra (fabushakra@crimson.ua.edu)

This work was supported in part by the National Oceanic and Atmospheric Administration (NOAA)/University Corporation for Atmospheric Research (UCAR) under Contract NA18NWS4620043B, and in part by NOAA/Cooperative Institute for Satellite Earth System Studies (CISESS) under Contract NA19NES4320002.

ABSTRACT This paper details a new approach for enhancing the radiation characteristics of a coplanar Vivaldi antenna (CVA) array. First, the inter-element mutual coupling is reduced by introducing slots in the conventional CVA array. Then, a low-profile dielectric patch antenna (DPA) is situated between the CVA flares when it acts as a traveling wave radiator at the higher frequency band. The DPA is excited by the loop current at the radiation part of the CVA, and a set of TE modes with omnidirectional radiation patterns are excited. This combination enhances the directivity in the broadside direction of the CVA and suppresses the grating lobes by as much as 10 dB. The 4×1 linear array covers the frequency range of 2.77-13.6 GHz, with 132% fractional bandwidth. Then, four of the proposed linear arrays are connected to constitute an 8×2 planar array to achieve a gain of 15.2-24.6 dBi. The proposed arrays are fabricated, tested, and mounted on a small unmanned aerial system (sUAS) for radar measurements. The real-life field radar results with the proposed arrays are presented including an echogram of the scanned area.

INDEX TERMS High gain antennas, radar applications, radiation pattern enhancement.

I. INTRODUCTION

Ultra-wideband (UWB) antennas with high gain are crucial components of modern communication systems, microwave imaging, high-speed wireless communications, and remote sensing radars. Modern radar systems such as UWB frequency modulated continuous wave (FMCW) radars require a broad bandwidth for fine range resolution to obtain high-quality radar images [1]. In addition, FMCW radars are being used for different remote sensing applications and target detection [2], [3]. Recently, radars integrated on sUAS have been widely used for various applications, including measuring soil moisture and ice thickness due to their cost-effectiveness and installation flexibility [4], [5]. The major requirements in designing antennas for a low-power and high-sensitivity sUAS radar are to enable ultra-wide bandwidth and high gain while maintaining a lightweight and an aerodynamic structure. For accurate backscatter measurements, the radiation pattern must also be symmetric with low side lobes over the operating frequency range. Several types of antennas have been studied to fulfill these requirements. The Vivaldi antenna can have as wide as 22:1 impedance bandwidth [6], [7]. However, the main challenge in designing a Vivaldi antenna is maintaining stable radiation patterns at the higher end of the operating frequency band, where the antenna works as a traveling wave radiator. Langley *et al.* [8] introduced the balanced antipodal Vivaldi antenna (BAVA) with two slots on opposite sides of the

The associate editor coordinating the review of this manuscript and approving it for publication was Sandra Costanzo.

substrate to improve the radiation performance of the CVA. Subsequently, a few other methods were reported to improve the antipodal Vivaldi antenna (AVA) radiation performance, for instance, by adding small resonator cells [9]–[12] or a parasitic elliptical patch [13] in the flared aperture to improve the gain. Nevertheless, these require increasing the size of the substrate significantly to situate these extra resonators. Zhu *et al.* [14] presented a linear AVA array with a metasurface located at the aperture without extending the substrate size. The gain showed an average of 2 dBi improvement, though it came at the expense of a high sidelobe level (SLL) for 16.5% of the impedance bandwidth. In a similar approach, Liu *et al.* [15] placed a triangular patch on the two sides of the AVA array's aperture substrate. The gain improved at the higher end of the bandwidth, but it had an asymmetric SLL. In addition, creating slots in the geometry of a Vivaldi antenna was reported to improve bandwidth, gain, and radiation pattern. Fei *et al.* [16], Oliveira *et al.* [17], Liu *et al.* [18], and Abbak *et al.* [19] showed that corrugated edges and multiple slots could improve antenna bandwidth and gain. However, the effect at the array level was not reported. Nurhayati *et al.* [20] showed that corrugated slots at the end of the Vivaldi antenna's edges could improve the mutual coupling between the array elements. However, their array's radiation patterns showed a high sidelobe level after the center of the operating band. Also, Zhu *et al.* [21] proposed a method to reduce the mutual coupling for the AVA array by adding multiple notches in the ground plane. However, this resulted in grating lobes distortion.

Alternatively, a dielectric lens can improve the radiation pattern of a Vivaldi antenna by extending the end portion of the substrate into different shapes, e.g., circular, triangular, or trapezoidal [22]–[24]. The drawback is that the antenna's footprint needs to be increased accordingly, as the directivity depends on the size of the dielectric lens. Furthermore, the lens material is the same as the antenna substrate, which usually has a low dielectric constant to widen the bandwidth. A few studies reported using a higher permittivity dielectric lens in the radiation aperture to concentrate the energy more towards the center. Bourqui *et al.* [25], Juan *et al.* [26], and Amiri *et al.* [27] proposed a modified BAVA by creating an aperture in the antenna substrate and inserting a higher permittivity dielectric material in the created gap to improve the directivity. A multi-layer dielectric lens was also inserted in front of the antenna aperture [28]. However, creating an aperture in the substrate and filling it with another dielectric material adds more complexity to the fabrication process and causes phase velocity variation for the electromagnetic waves traveling towards the end of the aperture.

Another reported approach [29], [30] surrounded the Vivaldi antenna with either a low dielectric constant material or a 3D phase lens to improve the gain and radiation performance. Also, a 3D massive dielectric lens was added at the aperture end of the Vivaldi antenna [31]. These 3D surrounding materials improved the gain and radiation pattern with SLL suppression. Unfortunately, its bulky size and heavyweight limit this approach's benefits in a large array environment.

On the other hand, the dielectric resonator antenna (DRA) is a 3D antenna with one more degree of freedom compared to microstrip patch antennas. This feature provides the ability to excite the desired mode and radiation pattern that cannot be generated with a 2D patch antenna. Also, the DRA radiation efficiency is higher than that of 2D antennas. However, the DRA profile is unsuitable if low-profile antennas are required. Thus, the dielectric patch antenna (DPA) is a compromise between the DRA and the microstrip patch antenna. The DPA is a low-profile DRA with a ratio of the maximum edge length to the height of 10 or more. Recently, Lai *et al.* [32] and Wang *et al.* [33] designed a narrow band DPAs and showed that these radiators could achieve more than 5 dBi gain with high efficiency even with a high dielectric material with a permittivity of 90. On the other hand, Tang *et al.* [34], proposed another PDA design with an extended bandwidth of 20%.

This paper presents a combined antenna array design of a CVA with a low-profile DPA for directivity improvement. The paper is organized as follows. Section II describes the ultra-wideband CVA linear array with a 4×1 arrangement. The slots' effects on the mutual coupling and the E-plane grating lobes suppression at higher frequencies are presented. Section III discusses the DPA shape effect on focusing the radiation toward the desired direction, and the analysis of the modes for the DPA is shown. Section IV presents four linear arrays used to form a planar 8×2 array for radar measurements. The planar array simulated and measured results are presented. Section V reports a real-field radar test using the proposed antenna on a sUAS. Finally, a conclusion is given in Section VI.

II. CVA LINEAR ARRAY DESIGN

Fig. 1(a) shows the conventional 4×1 CVA array designed on a Rogers RO3003 substrate with relative permittivity and thickness of 3 and 0.762 mm, respectively.

Both tapered edges of the antenna are on the top side of the substrate, while the power divider is on the back side. The input impedance of the single antenna is approximately 100 Ω, and the multi-stage power divider makes a smooth transition to the 50 Ω port. The Vivaldi tapered equation is given by (1):

$$y = Sve^{-xt} + C_1 \tag{1}$$

where, S is the half throat width of the antenna and is equal to 0.35 mm, t is the exponential tarped factor and equal to 84, $C_1 = 19.1$ mm, ($0 \text{ mm} \leq x \leq 33.9$ mm) and $v = \pm 1$.

The CVA dimensions W and L are 186 and 93 mm, while the dimensions of the DPA are d, W_d, r_d, W_1, and L_1 which correspond to 21, 20, 7.8, 3, and 15 mm, respectively. At the lower end of the CVA, an elliptical gap is created with major and minor axes of 7 and 3 mm, respectively.

Mutual coupling degrades the overall gain of the array due to the out-of-phase current distribution of the unwanted

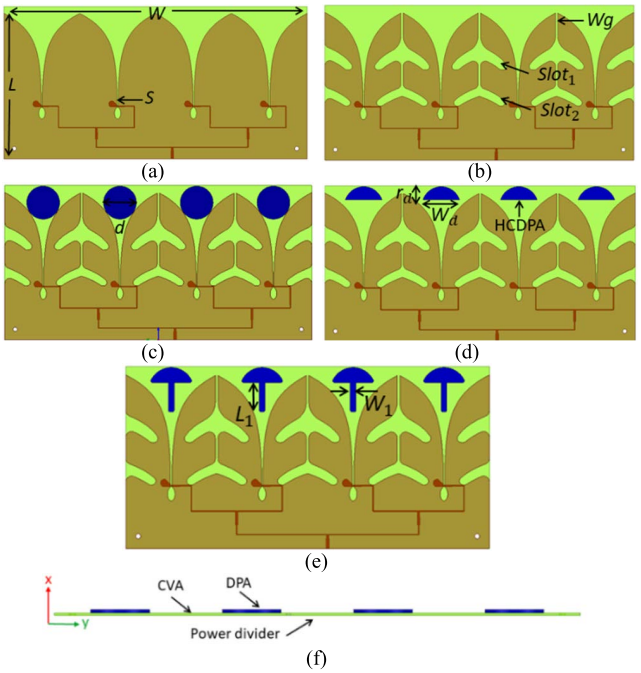

FIGURE 1. Development of the CVA array. (a) Conventional CVA (Ant I) (b) CVA with slots (Ant II) (c) CVA with CDPA (Ant III) (d) CVA with HCDPA (Ant IV) (e) umbrella-shaped DPA (Ant V) (f) Side view (Ant V).

waves traveling between adjacent elements. The mutual coupling can be reduced by increasing the distances between elements, but this causes higher grating lobes, especially in UWB antennas, where the distance between the elements exceeds 2 λ_g. In general, the spacing between the elements (W_e) is given by (2).

$$W_e < \frac{\lambda g}{1 + |\cos \varphi|} \tag{2}$$

where, φ is the angle of the main beam. The grating lobes increase when the spacing between the elements exceeds one guided wavelength for the broadside radiation. On the other hand, a larger spacing leads to a narrower main beam in the radiation patterns, which is beneficial in radar applications. Notably, in the CVA E-plane, traveling waves between elements on the same substrate significantly affect the array's performance. This effect can be reduced by creating a narrow gap ($W_g = 1$ mm) between the elements, as illustrated in Fig. 1(b). Subsequently, two slots are created with an exponential taper to each flare of the single antenna. Each slot has different optimized variables to improve the matching. The separation between the centers of slots is 20.1 mm. The corner edges in the design are smoothed to minimize unwanted wave diffraction that affects the return loss. The slots equations are given by (3).

$$\text{Slot}_{1,2} = C_2 u e^{-kt} \tag{3}$$

where for slot$_1$, $C_2 = 0.8$ mm, $t = 116.4$, (19.5 mm $\leq k \leq$ 40 mm) and ($-0.55 \leq u \leq 1.25$), while $C_2 = 0.95$ mm and $t = 125$ for slot$_2$.

The radiation patterns of the CVA array are improved by placing a cylindrical DPA (CDPA) at the end of the flared aperture of each element, as shown in Fig. 1(c). The CDPA material is TMM10 with relative permittivity of 9.2, diameter (d) of 22 mm, and thickness (h) of 1.27 mm. The DPA is coupled through the electric field distribution of the radiation aperture in the Vivaldi antenna. In Fig. 1(d), the CDPA is cut slightly above the center to form a half-CDPA (HCDPA). Finally, in Fig. 1(e), an extension to the HCDPA is added to form an umbrella-shaped DPA. This geometry shows significant capabilities in directing the surface current and improving the array radiation patterns.

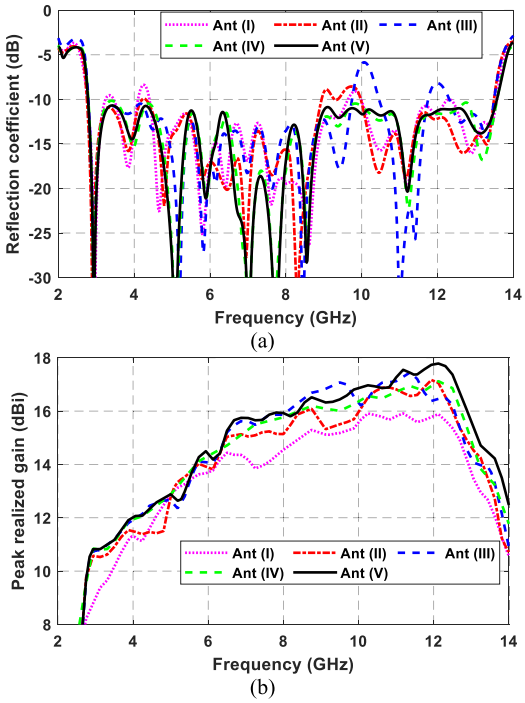

FIGURE 2. CVA development stages performance (a) reflection coefficient (b) peak realized gain.

The reflection coefficient for the final design covers the frequency band of 2.77-13.6 GHz, with 132% fractional bandwidth, as illustrated in Fig. 2(a). This bandwidth is sufficient for most UWB radar applications including snow thickness and soil moisture measurements [35], [36]. The gain value is shown in Fig. 2(b) and clearly improves once the slots are created between the adjacent elements. This result is expected as slots reduce the mutual coupling. The shape of slots is important as the stronger currents around them contribute in improving the gain. Notably, slot shapes and their locations in this design were optimized carefully to improve the gain over the entire frequency band as in some cases, slots may degrade the gain at specific frequencies [37], [38]. Both CDPA (Ant III) and HCDPA (Ant IV) show a slight improvement in the gain value, but the HCDPA improves the matching at the center of the operating band. The umbrella-shaped DPA shows improvement with an average of 1 to 2 dBi after $f = 7$ GHz, where the gain of the final design varies from 10.8-17.8 dBi.

The DPA shape is important as the electric field coupling between the CVA and the DPA depends on the position and the occupied area of the DPA with respect to the maximum current intensity. The E-plane radiation patterns of the developed array show that the final design with the umbrella-shaped DPA improves the radiation patterns by suppressing the side lobes and grating lobes at higher frequencies between 5-8 dB, as shown in Fig. 3. As the gain value is improved, the half-power beamwidth (HPBW) becomes narrower by approximately 1 to 2 degrees at the higher frequency band. The DPA in the final design (Ant V) produces a very good symmetry in the side lobes as well as grating lobes around the main beam.

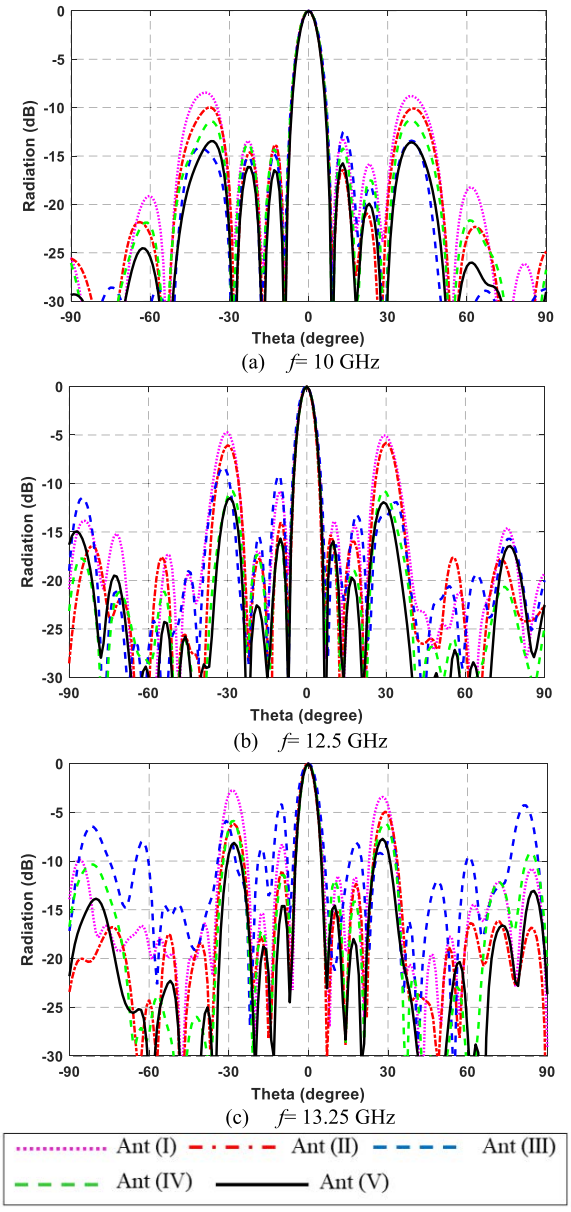

FIGURE 3. Co-polarized E-plane radiation patterns of the 4 × 1 CVA array.

In this design, the distance between the elements at the end of the frequency band exceeds 3.5 λ_g. Despite this large spacing, grating lobes and first sidelobes are 11 dB below the main lobe except at $f = 13.25$ GHz, where grating lobes are only about 9 dB below the main lobe. The slots in Ant (II) improve the grating lobes up to $f = 10$ GHz, where the inter-element spacing is about 2.5 λ_g. However, at higher frequencies with spacing between elements being much greater than a wavelength, the DPAs provide more suppression of grating lobes. The cross-polarization level and front-to-back (F/B) ratio are larger than 25 and 15 dB over the frequency range of interest, respectively. The full radiation patterns for the proposed design are presented in Section IV.

The low-profile DPA contributes to the CVA array's overall radiation after the cut-off frequency of the first mode, which is approximately 7 GHz. At this frequency, the CVA grating lobes increase until the end of the operating band. The higher permittivity material of the DPA causes the radiation pattern to be more focused towards the CVA end-fire direction with compact size. However, the fractional bandwidth will be narrower [39]. Based on that, the selected material for the DPA is TMM 10 with relative permittivity of 9.2. The DPA ceramic material has other advantages such as its availability, low dielectric loss at higher frequencies, and simplicity in fabrication.

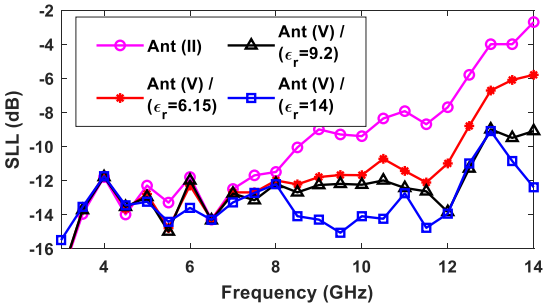

FIGURE 4. E-plane SLL for Ant (V) with different dielectric materials for the DPA.

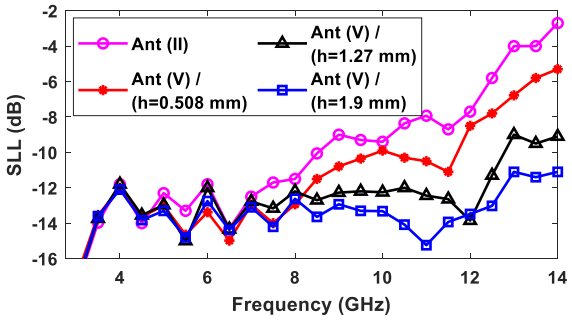

FIGURE 5. E-plane SLL for Ant (V) with different DPA height (*h*) in mm.

Figs. 4 and 5 present two parametric studies of the DPA material and height effects on the CVA radiation performance. Herein the figures, the SLL is defined as the difference between the main lobe's peak and the grating lobes' peak whether it is the first adjacent lobes or the farther grating lobes in the angular region of ±60° around the broadside direction. In Fig. 4, the SLL is compared for different DPA dielectric materials in Ant (V) and without the

DPA in Ant (II). As shown, without the DPA, the SLL reaches −2.7 dB at the higher end of the band. However, it can be suppressed to less than −12 dB with the higher permittivity material.

One of the advantages of using the DPA relative to the previously reported dielectric lens in the literature is that it avoids cutting the substrate and inserting another dielectric in the gap. This leads to a simplified fabrication process and reduction in the internal reflections of electromagnetic waves between two different boundaries. Basically, the phase velocity of the wave through the CVA substrate is constant. Another advantage of using this design is that it offers more flexibility in changing the DPA height to suppress the unwanted grating lobes further, as shown in Fig. 5. In most dielectric lens cases, the lens thickness is limited by substrate thickness.

However, there are two trade-offs for the DPA height that should be taken into consideration. First, even though the higher DPA will suppress the grating lobe (as illustrated in Fig. 5), the cross-polarization level will increase accordingly. This is due to the excitation of unwanted higher-order modes that alter the phase between the CVA fins. Secondly, the higher DPA height increases the weight of the overall array, which is one of the critical parameters for the sUAS applications. Based on the aforementioned factors, the DPA height is chosen between 1 and 1.5 mm.

III. DPA EXCITATION AND MODES ANALYSIS

This section discusses the theoretical concept and excitation mechanism of the DPA by examining the current distribution in the CVA array. The reasons for selecting the proposed DPA shape in Section (II) are also explained.

A. CDPA OMNIDIRECTIONAL RADIATION PATTERN

The CVA operates as a resonant antenna at the lower frequency band and radiates as a traveling wave radiator at higher frequencies. The electric current model at a given wavelength for an arbitrary Vivaldi antenna with a profile of $s(x)$ was reported by Chiappe *et al.* (4) [40]:

$$I(s(x)) = I_0 e^{\gamma s(x)} \times [\cos(k(s(x) - s(X))) + j\sin(k(s(x) - s(X)))] \quad (4)$$

where, γ is the attenuation coefficient, which is equivalent to $-t/p$ and p is the attenuation number for the antenna impedance. At higher frequencies, the current along the flared edge suffers from the phase reversal that degrades the radiation performance [13]. Fig. 6 illustrates the conceptual reversal current for the CVA with the corresponding current loop at the radiation aperture. The electric current along the CVA tapered flare can be represented by several electrically small segments along the edges. Each of these segments has horizontal (I_h) and vertical (I_v) current components [41]. The horizontal current is directed in two different directions on each fin at the higher frequencies due to the phase reversal. However, this is beneficial in creating the necessary condition to excite the TE modes in the cylindrical DPA (CDPA).

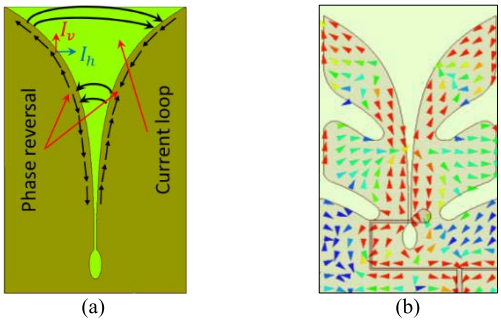

FIGURE 6. Conventional CVA current reversal at the higher frequencies (a) theoretical (b) simulation at $f = 7$ GHz.

In the previous studies, many attempts were reported to excite the $TE^{x}_{01\delta}$ and its higher-order modes such as the $TE^{x}_{011+\delta}$ mode in the cylindrical DRA (CDRA), where the ratio between the diameter (d) and thickness (h) is less than 10. Normally, it is difficult to achieve a uniform current loop over a wide bandwidth because of its small radiation resistance. Accordingly, the impedance matching of the CDRA for the omnidirectional modes is limited to a narrow band. Also, it requires a complex feeding structure underneath the DRA to excite these modes [42]– [45].

Similar to the DRA, the low-profile DPA can radiate with the TE mode once the appropriate excitation is applied with less variation on the profile axis. The current loop in the CVA aperture, however, offers a uniform current loop distribution at higher-order modes with wide bandwidth which excites the CDPA TE modes with an omnidirectional radiation pattern. These modes have a horizontal-polarized omnidirectional radiation pattern that improves the E-plane radiation without degrading the H-plane radiation of the CVA, as the null of the CDPA radiation is at the CVA H-plane direction. The CDPA in (Ant III) is considered first for the mode analysis. This is to simplify analyzing the electric field distribution for the different modes using the basic shape.

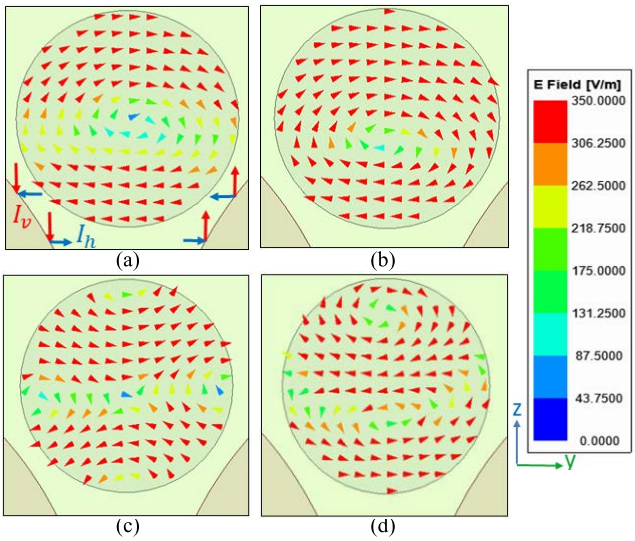

FIGURE 7. Electric field distribution of the CDPA (a) $f = 7.5$ GHz. (b) $f = 9$ GHz (c) 11 GHz (d) 13.25 GHz.

The electric field vector for the CDPA is shown at different frequencies in Fig. 7. At 7.5 and 9 GHz, the omnidirectional $TE^{x}_{01\delta}$ mode is propagating as expected. The proposed design excites the $TE^{x}_{01\delta}$ mode for the frequency range of 7.5-10.5 GHz, with more than 30% of impedance bandwidth. Also, the higher-order $TE^{x}_{011+\delta}$ mode can be excited if a cylindrical DRA is situated with a d/h ratio less than 10 [44]. Another advantage of this method is that the resonance mode in the CDPA is purely from the DPA itself as there is no embedded feeding network underneath the DPA. Normally, the feeding network will have another resonance frequency within the DPA operating band, which leads to a higher cross-polarization level. After 10.5 GHz, the other omnidirectional mode is the TE^{x}_{121} mode [46].

B. CDPA SHAPE ADJUSTMEN

By examining the electric field distribution in the CDPA, one expects that the radiation pattern can be focused in different directions on the *yz*-plane. It is clear that the +z axis is the desired direction to support the CVA end-fire pattern. Radiation in other directions degrades the performance as it generates an opposite wave traveling towards the throat of the CVA. This opposing wave performs like a multi-reflection in the overall antenna geometry and degrades the antenna match. Therefore, the shape of the CDPA was adjusted by maintaining the upper half of the dielectric loading as shown in Section II. The electric field distribution for the proposed DPA in Ant (V) is plotted in Fig. 8. Using the final DPA geometry, the maximum electric field focuses the electromagnetic waves to improve the CVA array directivity in the end-fire direction. The modes of the proposed DPA have a similar electric field distribution as the CDPA in Fig. 7.

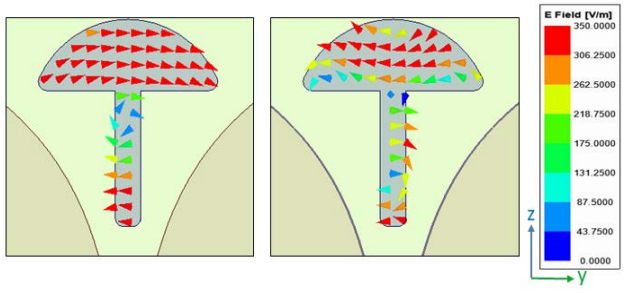

FIGURE 8. Electric field distribution of the proposed DPA (a) $f = 9$ GHz (b) $f = 13.25$ GHz.

IV. CVA PLANAR ARRAY DESIGN AND MEASUREMENTS

To increase the penetration of the radar signal through a lossy dielectric target (e.g., soil or ice), a high-gain antenna with a narrow HPBW in the along-track direction is needed to limit the Doppler bandwidth of a fast-moving platform [47]. Thus, four linear arrays are used to form a 16-element planar array with an 8 × 2 arrangement, as shown in Fig. 9, to obtain narrow beamwidth and to increase the radar power-aperture product. The total dimension of the array is 377 × 40 × 93 mm^3. The linear CVA arrays are separated by a small gap of 5 mm in the y-direction. This small gap suppresses the traveling waves between the adjacent linear CVA arrays and provides 20 dB or better isolation between the two arrays along the y-direction.

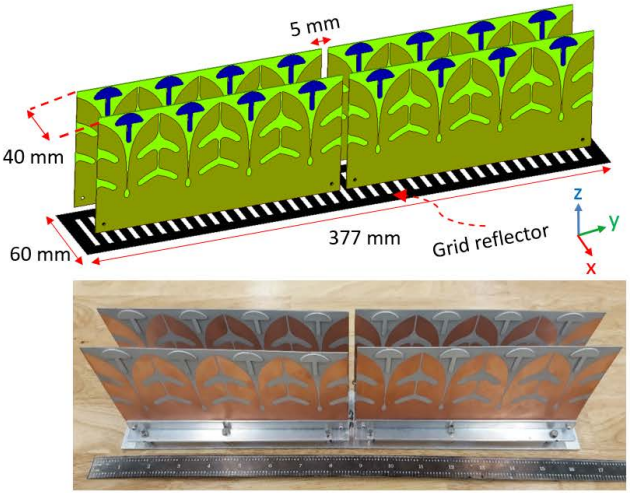

FIGURE 9. Proposed (8 × 2) planar CVA array with the low-profile DPA.

The lightweight is an essential requirement for the antennas for sUAS radar applications. The sUAS power consumption and maximum flight time strongly depend on the total payload. Previously, Vivaldi arrays using an aluminum sheet were reported to have wider bandwidth compared to the PCB CVA arrays [48]–[50]. Even though wide bandwidths were achieved, the weight of thick metal sheets limits the range of operation of the sUAS.

Herein, the linear CVA array has a total weight of 50 g including the SMA connector and the DPAs. The single DPA has a minimal effect on the overall array weight as it only weighs approximately 3 g. The overall weight of the entire planar array is 200 g, which is desirable for sUAS applications. The CVA arrays are mounted on a thin aluminum sheet of 0.8 mm thickness. Rectangular slots of 5 mm width were created in the aluminum sheet to reduce the aerodynamic air resistance relative to a solid sheet while improving the F/B ratio.

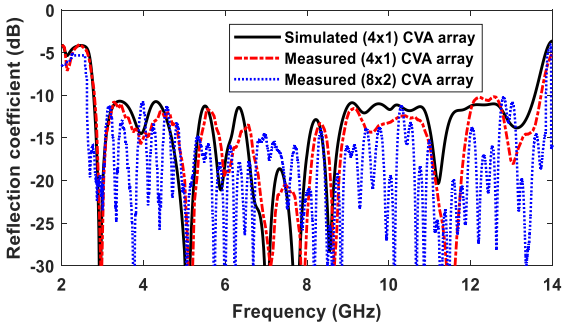

FIGURE 10. Reflection coefficients of the linear and planar CVA arrays.

The reflection coefficients of the CVA linear and planar arrays are shown in Fig. 10. The total bandwidth of the

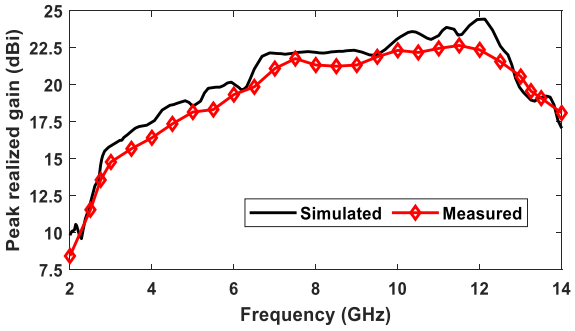

FIGURE 11. Peak realized gain of the 8 × 2 planar CVA array.

planar array is similar to the linear CVA array, and the multi resonances in the planar array are due to the presence of an external power divider and cables. The planar array gain is measured in the anechoic chamber after compensating for the insertion loss of the power divider and cables and it varies between 15.2 and 24.6 dBi, as shown in Fig. 11. Overall, there is a good agreement between measured and simulated results. The simulated and measured radiation efficiency of the proposed array is more than 90% over the entire band.

Fig. 12 shows the radiation patterns with a low SLL and grating lobes at higher frequencies, such as 12.5 GHz. The element spacing in the proposed CVA array is much greater than 0.5 λ at the higher frequency, which is the Nyquist sampling requirement to avoid the unwanted grating lobes [48]. This resulted in improving the overall gain value as the gain is directly proportional to the antenna aperture area. At the same time, the associated grating lobes are suppressed below 10 dB using the DPAs to perform radar measurements.

The traditional approaches to suppress the grating lobes by tapering the edge element of the array or using non-uniform spacing degrade the overall gain. However, in the proposed design, the gain is improved while the grating lobes are suppressed. Furthermore, the cross-polarization level is −25 dB at both planes through the entire band. The HPBW is varied from 13° to 2° and 60° to 14° for the E and H-plane, respectively. The F/B ratio is approximately 15-20 dB throughout the band.

In radar applications, it is preferable to maintain the F/B ratio as low as possible as in some cases the transmitter and receiver components are mounted on the back side of the antenna. The thin aluminum grid sheet at the back of the planar array improves the F/B ratio between 2-4 dB, as shown in Fig. 13. This improvement is similar to that obtained in [51] by creating multiple defected ground structure in the AVA ground plane. However, the only difference in this design is that the F/B improvement is consistent throughout the entire band while it was achieved at the higher frequencies in the mentioned reference.

Table 1 compares the proposed array with previous studies on this topic. It is clear that this design perfectly fulfills the sUAS radar requirements detailed in Section I.

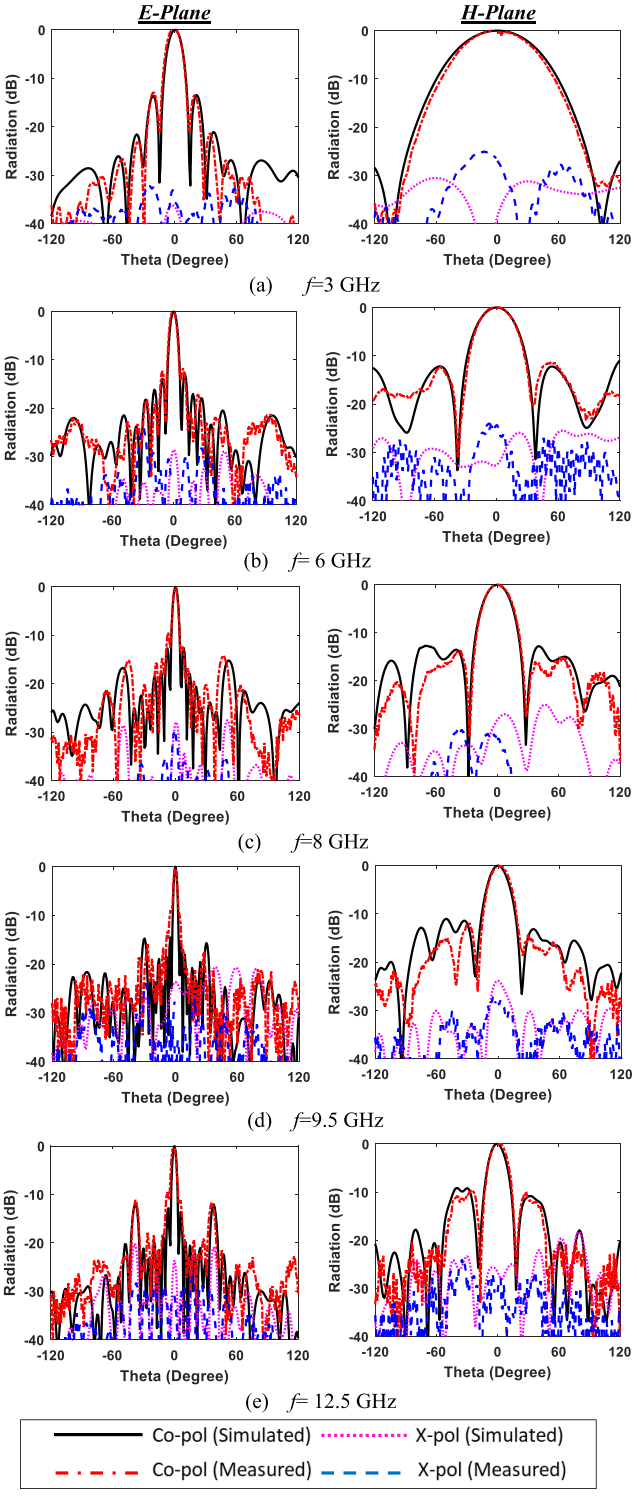

FIGURE 12. Radiation patterns for the proposed planar CVA array at different frequencies.

V. CVA TEST WITH sUAS RADAR

The CVA planar arrays are installed with an FMCW radar on an X6 multirotor drone manufactured by XFold, as shown in Fig. 14. The distance between the transmitter and receiver arrays is 130 cm to achieve isolation of 60 dB or better through the operating band. The isolation between the

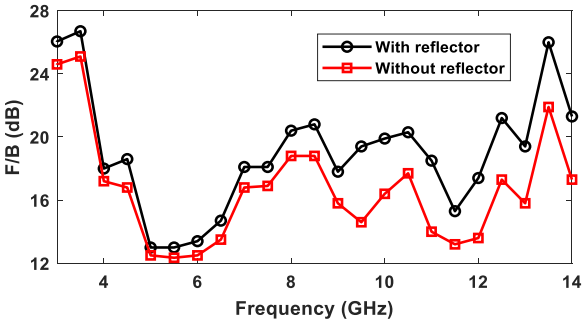

FIGURE 13. The Simulated front-to-back ratio for the planar CVA array.

TABLE 1. Comparison of the proposed array and literature.

Ref.	Array type	Array volume (λ_{low}^3)	Material / Thickness (mm)	Frequency (GHz) / BW (%)	Gain (dBi)
[14]	AVA 8×1	2.3×4.8×0.06	PCB/ 0.787 mm	24.1-28.5 16.5%	9.3-12
[15]	AVA 8×1	2.3×4.5×0.04	PCB/ 0.508 mm	24.7-27.5 11.3%	12.3-12.9
[21]	AVA 8×1	2.3×4.9×0.06	PCB/ 0.787 mm	24.55-28.5 14.8%	6.9-11.3
[38]	CVA 8×1	0.84×1.9×0.006	PCB/ 1.57 mm	1.2-4.2 111%	9-16
[48]	CVA 8×8	1.2×1.2×0.75	Aluminum/ 1.7 mm	10-35 111%	10-20.6
[50]	CVA 8×8	0.8×0.8×0.7	Aluminum/ 4 mm	2-18 160%	7-25
[This work]	CVA 4×1	0.85×1.7×0.007	PCB/ 0.762 mm	2.77-13.6 132%	10.8-17.8
[This work]	CVA 8×2	0.85×3.5×0.37	PCB/ 0.762 mm	2.77-13.6 132%	15.2-24.6

*λ_{low}: Free space wavelength at the lower frequency.

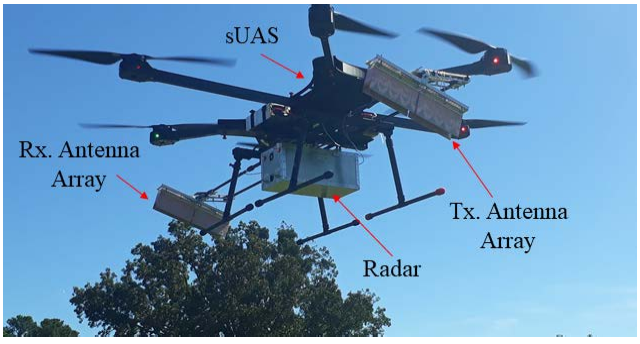

FIGURE 14. Proposed CVA array with low-profile DPA mounted on the sUAS for radar measurements.

transmitter and receiver arrays is extremely important in FMCW radars to prevent receiver saturation from the directly coupled transmitter signal. The E-plane of the proposed antenna is in the along-track direction, and the H-plane is in the cross-track direction. The antenna pointed 20° off the nadir for the experiment and was tested with different radar bands, e.g., at 2.8-3.55, 3.25-5.15, 2.8-5.8 GHz, and 4-7.785 GHz. The field tests for the CVA antenna with the radar system were performed at the Arboretum near The University of Alabama. The flight time on the drone varied between 20-30 minutes for different flights. The radar measurements are performed up to 100 m above the ground surface. From this height, the footprints of both antenna arrays overlapped. The average wind speed during the flight was 4-7 m/s. More details on the radar system are mentioned in [52]. The antenna showed exceptional performance with the different radar bands and weather conditions. The array is also used as a part of another UWB radar operating over the frequency range of 2.8-10.8 GHz on a manned aircraft with an average flight speed of 60 knots.

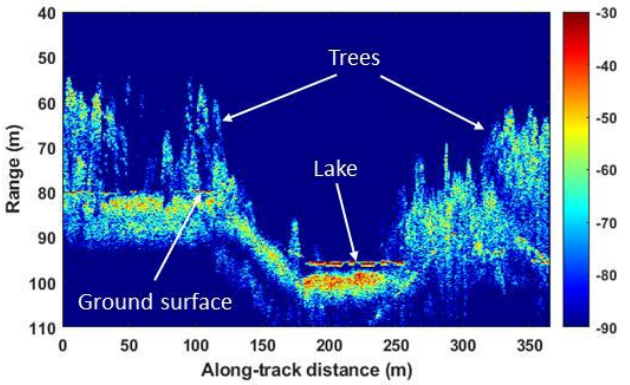

FIGURE 15. Echogram in dB-scale from the sUAS radar field measurements with the proposed CVA array.

Fig. 15 illustrates the echogram from FMCW radar operating over the frequency range from 3.25 to 5.15 GHz. The high gain antenna array allows operating the radar with a low transmit power of 10 dBm to avoid interference with systems operating at the same frequency range. The backscattered signal from the trees and ground surface collected by the receiver array is amplified, digitized, and stored for further processing. The collected data are processed with a fully focused SAR algorithm to improve the signal-to-noise ratio with a range resolution of 1 m [53], [54]. After that, four range profiles were incoherently integrated to improve the image quality. The image also clearly shows backscatters from the trees and ground surface. These data can be used to separate the backscatter from the ground and trees to estimate soil moisture as a function of distance along the flight path for bare and vegetation-covered ground. Algorithms to estimate soil moisture from the UWB radar are being developed.

VI. CONCLUSION

An ultra-wideband hybrid antenna design is presented in this paper. The new design exploits the DPA properties to enhance the radiation pattern characteristics of the coplanar Vivaldi antenna array. A low-profile and high permittivity DPA is placed on the top side of the Vivaldi antenna between the two radiating slots. The design shows that the CVA sidelobes and grating lobes can be reduced significantly by choosing the suitable DPA shape and exciting the appropriate DPA modes. Even though the spacing between the antennas is much greater than the guided wavelength, radiation patterns show a good directivity in the end-fire direction and can be used effectively for radar measurements. The proposed

design shows more enhancement in the radiation pattern at the higher frequency end of the band relative to the designs that used different types of slots and notches. Also, it is much easier in fabrication with more flexibility in selecting the design parameters. The CVA array is fabricated, tested, and mounted on a sUAS to support ultra-wideband FMCW radars for remote sensing of snow, soil moisture, and other targets.

ACKNOWLEDGMENT

The authors would like to thank the Remote Sensing Center (RSC) students and faculty at The University of Alabama for their valuable help in completing this work and also would like to thank Nathan Wagener for installing the antenna arrays on the sUAS, Tuan Luong for operating the sUAS to collect data, and Matthew Hargis for editing the paper.

REFERENCES

[1] F. Ulaby and G. D. Long, *Microwave Radar and Radiometric Remote Sensing*. Ann Arbor, MI, USA: The Univ. of Michigan Press, 2014.

[2] P. Kanagaratnam, T. Markus, V. Lytle, B. Heavey, P. Jansen, G. Prescott, and S. P. Gogineni, "Ultrawideband radar measurements of thickness of snow over sea ice," *IEEE Trans. Geosci. Remote Sens.*, vol. 45, no. 9, pp. 2715–2724, Sep. 2007.

[3] J.-B. Yan, S. Gogineni, F. Rodriguez-Morales, D. Gomez-Garcia, J. Paden, J. Li, C. J. Leuschen, D. A. Braaten, J. A. Richter-Menge, S. L. Farrell, J. Brozena, and R. D. Hale, "Airborne measurements of snow thickness: Using ultrawide-band frequency-modulated-continuous-wave radars," *IEEE Geosci. Remote Sens. Mag.*, vol. 5, no. 2, pp. 57–76, Jun. 2017.

[4] K. Wu, G. A. Rodriguez, M. Zajc, E. Jacquemin, M. Clément, A. De Coster, and S. Lambot, "A new drone-borne GPR for soil moisture mapping," *Remote Sens. Environ.*, vol. 235, Dec. 2019, Art. no. 111456.

[5] A. E.-C. Tan, J. McCulloch, W. Rack, I. Platt, and I. Woodhead, "Radar measurements of snow depth over sea ice on an unmanned aerial vehicle," *IEEE Trans. Geosci. Remote Sens.*, vol. 59, no. 3, pp. 1868–1875, Mar. 2021.

[6] J. Eichenberger, E. Yetisir, and N. Ghalichechian, "High-gain antipodal Vivaldi antenna with pseudoelement and notched tapered slot operating at (2.5 to 57) GHz," *IEEE Trans. Antennas Propag.*, vol. 67, no. 7, pp. 4357–4366, Jul. 2019.

[7] J. Bai, S. Shi, and D. W. Prather, "Modified compact antipodal Vivaldi antenna for 4–50-GHz UWB application," *IEEE Trans. Microw. Theory Techn.*, vol. 59, no. 4, pp. 1051–1057, Apr. 2011.

[8] J. D. S. Langley, P. S. Hall, and P. Newham, "Novel ultrawide-bandwidth Vivaldi antenna with low crosspolarisation," *Electron. Lett.*, vol. 29, no. 23, p. 2004, 1993.

[9] J. Zhang, S.-F. Liu, F. Wang, Z. Yang, and X.-W. Shi, "A compact high-gain Vivaldi antenna with improved radiation characteristics," *Prog. Electromagn. Res. Lett.*, vol. 68, pp. 127–133, 2017.

[10] L. Sang, X. Li, T. Chen, and G. Lv, "Analysis and design of tapered slot antenna with high gain for ultra-wideband based on optimisation of the metamaterial unit layout," *IET Microw., Antennas Propag.*, vol. 11, no. 6, pp. 907–914, May 2017.

[11] H. Cheng, H. Yang, Y. Li, and Y. Chen, "A compact Vivaldi antenna with artificial material lens and sidelobe suppressor for GPR applications," *IEEE Access*, vol. 8, pp. 64056–64063, 2020.

[12] J. Puskely, J. Lacik, Z. Raida, and H. Arthaber, "High-gain dielectric-loaded Vivaldi antenna for Ka-band applications," *IEEE Antennas Wireless Propag. Lett.*, vol. 15, pp. 2004–2007, 2016.

[13] I. T. Nassar and T. M. Weller, "A novel method for improving antipodal Vivaldi antenna performance," *IEEE Trans. Antenna Propag.*, vol. 63, no. 7, pp. 3321–3324, Jul. 2015.

[14] S. Zhu, H. Liu, and P. Wen, "A new method for achieving miniaturization and gain enhancement of Vivaldi antenna array based on anisotropic meta-surface," *IEEE Trans. Antennas Propag.*, vol. 67, no. 3, pp. 1952–1956, Mar. 2019.

[15] H. Liu, W. Yang, A. Zhang, S. Zhu, Z. Wang, and T. Huang, "A miniaturized gain-enhanced antipodal Vivaldi antenna and its array for 5G communication applications," *IEEE Access*, vol. 6, pp. 76282–76288, 2018.

[16] P. Fei, Y.-C. Jiao, W. Hu, and F.-S. Zhang, "A miniaturized antipodal Vivaldi antenna with improved radiation characteristics," *IEEE Antennas Wireless Propag. Lett.*, vol. 10, pp. 127–130, 2011.

[17] A. M. D. Oliveira, M. B. Perotoni, S. T. Kofuji, and J. F. Justo, "A palm tree antipodal Vivaldi antenna with exponential slot edge for improved radiation pattern," *IEEE Antennas Wireless Propag. Lett.*, vol. 14, pp. 1334–1337, 2015.

[18] Y. Liu, W. Zhou, S. Yang, W. Li, P. Li, and S. Yang, "A novel miniaturized Vivaldi antenna using tapered slot edge with resonant cavity structure for ultrawideband applications," *IEEE Antennas Wireless Propag. Lett.*, vol. 15, pp. 1881–1884, 2016.

[19] M. Abbak, M. N. Akinci, M. Çayören, and I. Akduman, "Experimental microwave imaging with a novel corrugated Vivaldi antenna," *IEEE Trans. Antennas Propag.*, vol. 65, no. 6, pp. 3302–3307, Feb. 2017.

[20] G. Hendrantoro, T. Fukusako, and E. Setijadi, "Mutual coupling reduction for a UWB coplanar Vivaldi array by a truncated and corrugated slot," *IEEE Antennas Wireless Propag. Lett.*, vol. 17, no. 12, pp. 2284–2288, Dec. 2018.

[21] S. Zhu, H. Liu, Z. Chen, and P. Wen, "A compact gain-enhanced Vivaldi antenna array with suppressed mutual coupling for 5G mm Wave application," *IEEE Antennas Wireless Propag. Lett.*, vol. 17, no. 5, pp. 776–779, May 2018.

[22] K. Kota and L. Shafai, "Gain and radiation pattern enhancement of balanced antipodal Vivaldi antenna," *Electron. Lett.*, vol. 47, no. 5, p. 303, 2011.

[23] A. Molaei, M. Kaboli, S. A. Mirtaheri, and M. S. Abrishamian, "Dielectric lens balanced antipodal Vivaldi antenna with low cross-polarisation for ultra-wideband applications," *IET Microw., Antennas Propag.*, vol. 8, no. 14, pp. 1137–1142, Nov. 2014.

[24] M. Moosazadeh, S. Kharkovsky, and J. T. Case, "Microwave and millimetre wave antipodal Vivaldi antenna with trapezoid-shaped dielectric lens for imaging of construction materials," *IET Microw., Antennas Propag.*, vol. 10, no. 3, pp. 301–309, Feb. 2016.

[25] J. Bourqui, M. Okoniewski, and E. C. Fear, "Balanced antipodal Vivaldi antenna with dielectric director for near-field microwave imaging," *IEEE Trans. Antennas Propag.*, vol. 58, no. 7, pp. 2318–2326, Jul. 2010.

[26] L. Juan, F. Guang, Y. Lin, and F. Demin, "A modified balanced antipodal Vivaldi antenna with improved radiation characteristics," *Microw. Opt. Technol. Lett.*, vol. 55, no. 6, pp. 1321–1325, Jun. 2013.

[27] M. Amiri, F. Tofigh, A. Ghafoorzadeh-Yazdi, and M. Abolhasan, "Exponential antipodal Vivaldi antenna with exponential dielectric lens," *IEEE Antennas Wireless Propag. Lett.*, vol. 16, pp. 1792–1795, 2017.

[28] D. Huang, H. Yang, Y. Wu, F. Zhao, and X. Liu, "A high-gain antipodal Vivaldi antenna with multi-layer planar dielectric lens," *J. Electromagn. Waves Appl.*, vol. 32, no. 4, pp. 403–412, Mar. 2018.

[29] M. Moosazadeh, "High-gain antipodal Vivaldi antenna surrounded by dielectric for wideband applications," *IEEE Trans. Antennas Propag.*, vol. 66, no. 8, pp. 4349–4352, Aug. 2018.

[30] L. Sang, S. Wu, G. Liu, J. Wang, and W. Huang, "High-gain UWB Vivaldi antenna loaded with reconfigurable 3-D phase adjusting unit lens," *IEEE Antennas Wireless Propag. Lett.*, vol. 19, no. 2, pp. 322–326, Feb. 2020.

[31] R. Cicchetti, V. Cicchetti, A. Faraone, and O. Testa, "A class of lightweight spherical-axicon dielectric lenses for high gain wideband antennas," *IEEE Access*, vol. 9, pp. 151873–151887, 2021.

[32] H. W. Lai, K.-M. Luk, and K. W. Leung, "Dense dielectric patch antenna—A new kind of low-profile antenna element for wireless communications," *IEEE Trans. Antennas Propag.*, vol. 61, no. 8, pp. 4239–4245, Aug. 2013.

[33] X.-Y. Wang, S.-C. Tang, X.-F. Shi, and J.-X. Chen, "A low-profile filtering antenna using slotted dense dielectric patch," *IEEE Antennas Wireless Propag. Lett.*, vol. 18, no. 3, pp. 502–506, Mar. 2019.

[34] S.-C. Tang, X.-Y. Wang, W.-W. Yang, and J.-X. Chen, "Wideband low-profile dielectric patch antenna and array with anisotropic property," *IEEE Trans. Antennas Propag.*, vol. 68, no. 5, pp. 4091–4096, May 2020.

[35] S. Gogineni, K. Wong, S. Krishnan, P. Kanagaratnam, T. Markus, and V. Lytle, "An ultra-wideband radar for measurements of snow thickness over sea ice," in *Proc. IEEE Int. Geosci. Remote Sens. Symp. (IGARSS)*, Jul. 2003, pp. 2802–2804, doi: 10.1109/IGARSS.2003.1294591.

[36] C. D. Simpson, S. Kolpuke, A. K. Awasthi, T. Luong, S. Memari, S. Yan, R. Taylor, J. Larson, and P. Clement, "Development of a UAS-based ultra-wideband radar for fine-resolution soil moisture measurements," in *Proc. IEEE Radar Conf. (RadarConf)*, May 2021, pp. 1–4.
[37] M. Moosazadeh and S. Kharkovsky, "A compact high-gain and front-to-back ratio elliptically tapered antipodal Vivaldi antenna with trapezoid-shaped dielectric lens," *IEEE Antennas Wireless Propag. Lett.*, vol. 15, pp. 552–555, 2016.
[38] Y. Yang, Y. Wang, and A. E. Fathy, "Design of compact Vivaldi antenna arrays for UWB see through wall applications," *Prog. Electromagn. Res.*, vol. 82, pp. 401–418, 2008.
[39] T. A. Denidni and Z. Weng, "Rectangular dielectric resonator antenna for ultra-wideband applications," *Electron. Lett.*, vol. 45, no. 24, pp. 1210–1212, 2009.
[40] M. Chiappe and G. L. Gragnani, "Vivaldi antennas for microwave imaging: Theoretical analysis and design considerations," *IEEE Trans. Instrum. Meas.*, vol. 55, no. 6, pp. 1885–1891, Dec. 2006.
[41] J. T. Logan, R. W. Kindt, and M. N. Vouvakis, "Low cross-polarization Vivaldi arrays," *IEEE Trans. Antennas Propag.*, vol. 66, no. 4, pp. 1827–1837, Apr. 2018.
[42] T. Liu, H. Yang, Y. He, and J. Lu, "A $TE_{01\delta}$ mode omnidirectional dielectric resonator antenna excited by a special configuration," *IEEE Trans. Antennas Propag.*, vol. 66, no. 12, pp. 7339–7341, Aug. 2018.
[43] B. R. Motlhabane and D. Gray, "TE-monopole radiation pattern DRA for UAVs," in *Proc. Int. Symp. Antennas Propag. (ISAP)*, 2012, pp. 499–502.
[44] W. Li, K. W. Leung, and N. Yang, "Omnidirectional dielectric resonator antenna with a planar feed for circular polarization diversity design," *IEEE Trans. Antennas Propag.*, vol. 66, no. 3, pp. 1189–1197, Mar. 2018.
[45] X. Liu, K. W. Leung, and N. Yang, "Wideband horizontally polarized omnidirectional cylindrical dielectric resonator antenna for polarization reconfigurable design," *IEEE Trans. Antennas Propag.*, vol. 69, no. 11, pp. 7333–7342, Nov. 2021, doi: 10.1109/TAP.2021.3076458.
[46] Y. M. Pan, K. W. Leung, and K. Lu, "Study of resonant modes in rectangular dielectric resonator antenna based on radar cross section," *IEEE Trans. Antennas Propag.*, vol. 67, no. 6, pp. 4200–4205, Jun. 2019.
[47] C. Liu, M. T. A. Qaseer, and R. Zoughi, "Influence of antenna pattern on synthetic aperture radar resolution for NDE applications," *IEEE Trans. Instrum. Meas.*, vol. 70, 2021, Art. no. 8000911.
[48] M. A. Elmansouri, G. R. Friedrichs, L. B. Boskovic, and D. S. Filipovic, "An v-band through Ka-band thinned all-metal vivaldi phased array," *IEEE Trans. Antennas Propag.*, vol. 69, no. 11, pp. 7613–7623, Nov. 2021, doi: 10.1109/TAP.2021.3076680.
[49] R. W. Kindt and W. R. Pickles, "Ultrawideband all-metal flared-notch array radiator," *IEEE Trans. Antennas Propag.*, vol. 58, no. 11, pp. 3568–3575, Nov. 2010.
[50] J.-B. Yan, S. Gogineni, B. Camps-Raga, and J. Brozena, "A dual-polarized 2–18-GHz Vivaldi array for airborne radar measurements of snow," *IEEE Trans. Antennas Propag.*, vol. 64, no. 2, pp. 781–785, Feb. 2016.
[51] S. Zhu, H. Liu, P. Wen, Z. Chen, and H. Xu, "Vivaldi antenna array using defected ground structure for edge effect restraint and back radiation suppression," *IEEE Antennas Wireless Propag. Lett.*, vol. 19, no. 1, pp. 84–88, Jan. 2020.
[52] F. Abushakra, N. Jeong, D. N. Elluru, A. K. Awasthi, S. Kolpuke, T. Luong, O. Reyhanigalangashi, D. Taylor, and S. P. Gogineni, "A miniaturized ultra-wideband radar for UAV remote sensing applications," *IEEE Microw. Wireless Compon. Lett.*, vol. 32, no. 3, pp. 198–201, Mar. 2022, doi: 10.1109/LMWC.2021.3129153.
[53] M. A. Richards, *Fundamentals of Radar Signal Processing*. New York, NY, USA: McGraw-Hill, 2005.
[54] J. Gray, *Stimson's Introduction to Airborne Radar*, 3rd ed. U.K.: SciTech, 2014.

FERAS ABUSHAKRA received the B.Sc. degree in electrical engineering from the Jordan University of Science and Technology (JUST), Irbid, Jordan, and the M.Sc. degree in wireless communication engineering from Al-Yarmouk University, Jordan, in 2017. He is currently pursuing the Ph.D. degree in electrical and computer engineering with The University of Alabama (UA), Tuscaloosa. He is also a Graduate Research Assistant with the Remote Sensing Center, UA. His research interests include UWB arrays, waveguides, and radar systems for earth remote sensing, including soil moisture and snow depth measurements.

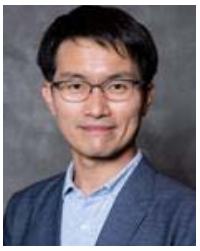

NATHAN JEONG (Senior Member, IEEE) received the Ph.D. degree in electrical and computer engineering from Purdue University, in 2010. At 2018, he joined The University of Alabama as an Assistant Professor. His current research interests include 5G millimeter-wave antenna and systems, adaptive RF front-ends, and electromagnetics. He has total of 12 years of industrial experience at Samsung Electronics, BlackBerry, and Qualcomm. In addition, he holds more than 60 international patent and patent applications in the areas of antennas, wireless communication circuit, microwave and millimeter wave systems, V2X (vehicle to everything), wireless power transfer, and bioelectronics.

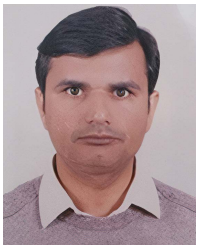

ABHISHEK K. AWASTHI (Member, IEEE) received the B.Tech. degree in electronics and communication engineering from the Ajay Kumar Garg Engineering College Ghaziabad (UPTU), Lucknow, in 2008, the M.Tech. degree in digital communication from the Ambedkar Institute of Technology Delhi (GGSIP University Delhi), in 2011, and the Ph.D. degree in RF and microwave from the Department of Electrical Engineering, Indian Institute of Technology Kanpur, in 2018. Currently, he is an Assistant Research Engineer with the Remote Sensing Center, The University of Alabama, Tuscaloosa. His current research interests include phased antenna arrays and ultra-wideband radar systems.

SHRINIWAS KOLPUKE (Graduate Student Member, IEEE) received the B.Sc. degree in electronics engineering from Swami Ramanand Teerth Marathwada University Nanded, India, in 2011, the Master of Science degree in VLSI and embedded system design from Jawaharlal Nehru Technological University Hyderabad, India, in 2013, and the Master of Science degree in aerospace engineering with the University of Kansas, Lawrence, in 2017. He is currently pursuing the Ph.D. degree in aerospace engineering and mechanics with The University of Alabama, Tuscaloosa. His research interests include design, development, and optimization of FMCW radars for snow measurements.

CHRISTOPHER SIMPSON received the B.S. degree in aeronautics and astronautics engineering from Purdue University, in 2010, and the M.S. degree in aerospace engineering and mechanics from The University of Alabama, in 2016, where he is currently pursuing the Ph.D. degree in aerospace engineering and mechanics.

OMID REYHANIGALANGASHI (Graduate Student Member, IEEE) received the B.Sc. degree in electrical engineering from Karaj Islamic Azad University, Alborz, Iran, in 2014, and the M.Sc. degree in electrical engineering from Qazvin Islamic Azad University, Qazvin, Iran, in 2017. He is currently pursuing the Ph.D. degree in electrical engineering with the School of Electrical and Computer Engineering, University of Alabama, with a Research Assistantship (RA). From 2015 to 2019, he worked as a Project Engineer at FiberHome Telecommunication Technologies Company Ltd., a globally renowned information and communication network product and solution provider. His research interests include field-programmable gate array (FPGA), digital signal processing (DSP), and embedded systems.

DEEPAK N. ELLURU (Graduate Student Member, IEEE) received the bachelor's degree in electronics and communication engineering in India, and the master's degree from The University of Alabama, Huntsville, in 2018. He is currently pursuing the Ph.D. degree. He joined the Remote Sensing Center, The University of Alabama, in 2019. His research interests include microwave circuits, antenna design, and microwave remote sensing.

AABHASH BHANDARI is currently pursuing the B.Sc. degree in aerospace engineering and mechanics with The University of Alabama, Tuscaloosa. He is also working as an Undergraduate Research Assistant with the Remote Sensing Center, UA. His research interests include unmanned aircraft systems, hybrid powertrains, and GNC.

DREW TAYLOR (Member, IEEE) received the B.S. and M.S. degrees in electrical engineering from The University of Alabama, Tuscaloosa, AL, USA, in 2008 and 2011, respectively, and the Ph.D. degree in electrical and computer engineering from Mississippi State University, Mississippi State, MS, USA, in 2018. He is currently an Assistant Professor in electrical and computer engineering with the Remote Sensing Center, The University of Alabama. His research interests include embedded systems, radar signal processing, and remote sensing of the earth.

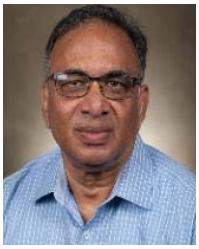

S. PRASAD GOGINENI (Life Fellow, IEEE) is currently a Cudworth Professor in engineering with The University of Alabama and the Director of the Remote Sensing Center. He was the Founding Director of the NSF Science and Technology Center for Remote Sensing of Ice Sheets (CReSIS), University of Kansas, from 2005 to 2016. He worked as the Manager of NASA's Polar Program, from 1997 to 1999. He received the Louise Byrd Graduate Educator Award with the University of Kansas and was a Fulbright Senior Scholar with the University of Tasmania, in 2002. He has been involved with radar sounding and imaging of ice sheets for approximately 35 years and contributed to the first successful demonstration of SAR imaging of an ice bed through ice more than 3 km thick. He is also led the development of ultra-wideband radars for measuring the thickness of snow over sea ice and the mapping of internal layers in polar firm and ice.